ARTICLE

Experimental and Numerical Investigation on the Aerodynamic Characteristics of High-Speed Pantographs with Supporting Beam Wind Deflectors

Shiyang Song[1,*] and Tongxin Han[2]

[1]Postgraduate Department, China Academy of Railway Sciences, Beijing, 100081, China

[2]Locomotive & Car Research Institute, China Academy of Railway Sciences Corporation Limited, Beijing, 100081, China

*Corresponding Author: Shiyang Song. Email: shiyangsong@rails.cn

ABSTRACT

Aiming to mitigate the aerodynamic lift force imbalance between pantograph strips, which exacerbates wear and affects the current collection performance of the pantograph-catenary system, a study has been conducted to support the beam deflector optimization using a combination of experimental measurements and computational fluid dynamics (CFD) simulations. The results demonstrate that the size, position, and installation orientation of the wind deflectors significantly influence the amount of force compensation. They also indicate that the front strip deflectors should be installed downwards and the rear strip deflectors upwards, thereby forming a "π" shape. Moreover, the lift force compensation provided by the wind deflectors increases with the size of the deflector. Alternative wind compensation strategies, such as control circuits, are also discussed, putting emphasis on the pros and cons of various pantograph types and wind compensation approaches.

KEYWORDS

High-speed pantograph; aerodynamic lift force; supporting beam wind deflectors; computational fluid dynamics (CFD)

Nomenclature

a	Acceleration
a_x	x component of measured acceleration
A	Area
C_L	Lift coefficient
F_f	Frictional force
F_L	Aerodynamic lift force
F_I	Pantograph impact force
F_S	Pantograph static lift force
F_x	x component of measured force
g	Gravitational coefficient
ρ	Fluid density
p	Fluid pressure
τ_{ij}	Stress tensor
μ	Coefficient of friction

μ_t Turbulent viscosity
μ_f Fluid dynamic viscosity

1 Introduction

The double-strip pantograph is a widely used type of pantograph for high-speed rail, with two carbon strips that are in contact with the overhead cables to deliver power to the locomotives. Despite the expectation of uniform contact force across each strip, achieving this is challenging due to complex aerodynamic effects. This leads to two issues that can impact the performance and longevity of the pantograph:

(1) Mechanically, a strip experiencing greater contact force experiences greater wear during its service life. This is because, based on Coulomb's law of friction, the frictional force is equal to the normal force multiplied by the coefficient of friction (see Eq. (1)). The two strips are expected to have the same coefficient of friction, but the one with a stronger aerodynamic lift force constantly works with more friction and wears out at a faster rate.

$$F_f = \mu F_L \tag{1}$$

where F_f is the frictional force, μ is the coefficient of friction, and F_L is the lift force on the pantograph strip.

(2) Electrically, contact impedance depends on how well the two surfaces make contact. Weaker contacts have lower resistance, resulting in more current passing through them. When the force is insufficient to keep the strips in contact with the overhead electrical cables, arcing may occur and cause damage to the pantograph-catenary system.

To mitigate the identified issues, wind deflectors are used to balance the aerodynamic forces acting on the pantograph. However, most studies have primarily addressed the general aerodynamics of pantographs. For instance, Pombo et al. [1] proposed a model to study aerodynamic forces on the pantograph-catenary system and found that wind loads tend to cause an increase in contact forces. AbdelGawad et al. [2] examined the aerodynamic noise of high-speed pantographs in different operating conditions and concluded that using elliptic-edge cross-section bars may reduce aerodynamic noise at the pantograph head. Li et al. [3] analyzed the pantograph aerodynamic noise distribution and discovered that airflow leads to amplification in sound pressure levels in the knuckle-upstream direction and attenuation in the knuckle-downstream direction. Tan et al. [4] investigated the aerodynamic noises of pantographs due to different pantograph angles and determined that near-field aerodynamic noises on the longitudinal symmetrical plane of pantographs are distributed at the lower arm, middle hinge joints, and bases. Yan et al. [5] explored the distribution of aerodynamic drag forces of high-speed pantographs with CFD simulation and established that the pressure drag of the strip and base contributes the most to aerodynamic drag forces. Cheng et al. [6] focused on the effects of tunnel buffer structures on the aerodynamic forces of high-speed pantographs and noted that both aerodynamic lift and drag fluctuations are decreased at the entrance and exit of tunnels with bell mouth or side-opening buffer structures. Dai et al. [7] analyzed the effect of the diameters of upper and lower arms on the aerodynamic lift force of high-speed pantographs and pointed out the relationship between changes in size of different arms and the aerodynamic lift force change in high-speed pantographs. Watroba [8] proposed a numerical model using ANSYS CFX to calculate the aerodynamic forces exerted on the pantograph and found that the drag coefficient at a working height of 3000 mm is approximately 118% higher than at 1000 mm. Vo-Van et al. [9] incorporated aerodynamic forces into the pantograph-catenary dynamic simulation and revealed that aerodynamic irregularities only affect the mean contact force. Shaltout et al. [10] explored the aerodynamic noise of a high-speed pantograph under various operational conditions and suggested that

the employment of an elliptic cross-section leads to a 23.1% decrease in the acoustic sound pressure when the pantograph operates at 250 km/h. Mitsumoji et al. [11] applied a flow control method to mitigate the aerodynamic noise generated by a pantograph panhead and showed that the air suction near the separation point minimizes the narrow band aerodynamic noise originating from the panhead. Siano et al. [12] undertook an aerodynamic and aeroacoustics analysis of a high-speed pantograph model to reduce aerodynamic noise and discussed the possibility to develop a new design of the pantograph for high-speed trains. Ikeda et al. [13] considered a low-noise pantograph characterized by its few components with smooth forms and verified that the aerodynamic noise was reduced through wind tunnel and line tests. Collina et al. [14] presented an active control method for high-speed pantographs and validated the viability of the presented control scheme through numerical simulation. Kim et al. [15] evaluated the influence of cavity flow control on the aerodynamic noise of high-speed pantographs and concluded that noise radiated from the sides and the top can be significantly reduced by rounding the cavity edges.

Some studies have specifically targeted double-strip pantographs, such as Li et al. [16], who studied the aerodynamic noise characteristics of high-speed pantographs with strip spacing ranging from 0 to 540 mm; Dai et al. [17], who analyzed the aerodynamic performance of high-speed pantographs with strip spacing between 100 and 700 mm; Dai et al. [18], who performed a numerical study on the aerodynamic performance of four different head shapes of pantographs; and Shi et al. [19], who conducted a numerical analysis on the aerodynamic noise generated by a simplified double-strip pantograph. However, these studies mainly focused on strip spacing, head shapes, and aerodynamic noise characteristics.

In contrast, research specifically targeting wind deflectors has been limited. Dai et al. [20] investigated the baffle angles of crossbar-mounted wind deflectors for optimal aerodynamic performance, but the type of wind deflectors, supporting beam deflectors, has not been thoroughly studied (Supporting beam deflectors can balance the force difference between the two strips, while crossbar deflectors are used for reducing aerodynamic lift when the pantograph travels in the knuckle-downstream direction (Maaß [21])). Furthermore, while some studies have addressed the aerodynamics of pantographs in general, there is a lack of research focusing on the optimization of supporting beam wind deflectors to balance the force difference between the two strips of double-strip pantographs.

As shown in Fig. 1, six independent deflectors are equipped on a double-strip pantograph, four located underneath the supporting beams (Nos. 1, 3, 4, 6) and two under the crossbar (Nos. 2 and 5).
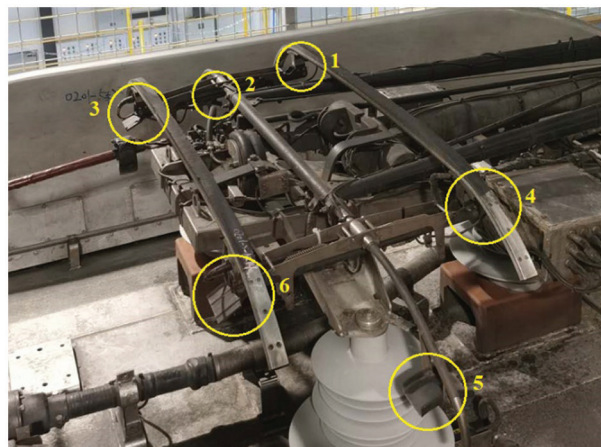

Figure 1: Locations of wind deflectors

Wind deflectors Nos. 3, 5, and 6 are visible in the photo, while the other three are obscured from view. A close-up shot is shown in Fig. 2.

(a) Supporting beam deflector   (b) Crossbar deflector

Figure 2: Two different types of wind deflectors

Some pantograph models may have additional or fewer deflectors. For example, the DSA380 has only two supporting beam deflectors instead of four. Older models may have an additional center wind adjuster, but it has become obsolete in the later models and is therefore not included in this study.

This study specifically focuses on the aerodynamic performance of the supporting beam deflectors during the knuckle-upstream direction travel, as high-speed trains use the rear pantograph more frequently for operation (illustrated in Fig. 3). The purpose of this study is to investigate the aerodynamic performance of the supporting beam deflectors and optimize their design to reduce the force difference between the two strips and improve the longevity and performance of the double-strip pantograph.
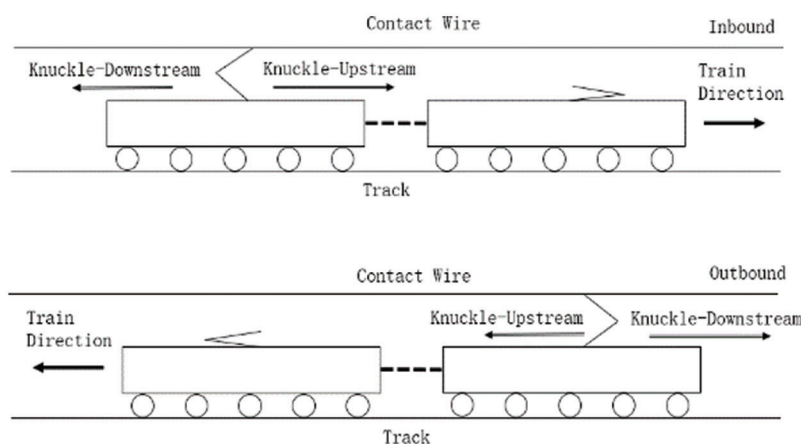

Figure 3: Operating direction

2 Experiment

To carry out the experimental investigation, the wind deflectors were initially removed from the supporting beams. A specific pantograph model featuring a single-arm double-strip structure was used,

rated voltage of 25 kV, current capacity of 1000 A, static lift force ranging from 70 to 120 N, and other relevant specifications as detailed in Table 1.

Table 1: Pantograph specifications

Properties	Values
Max. speed	420 km/h
Structure type	Single-arm, double-strip
Rated voltage	25 kV
Current capacity	1000 A
Static lift	70–120 N
Max. work height	2600 mm
Max. head length	1950 mm
Strip length	1060 mm
Strip spacing	580 mm

Four pressure sensors were installed, one at each end of the supporting beam, as shown in Fig. 4, to measure the total force acting on each strip. Four accelerometers were also installed next to the pressure sensors for measurement of acceleration. The use of accelerometers was deemed necessary to account for the impact force caused by vibration in addition to the aerodynamic force and static lift of the pantograph. This vibration can be harmonic or irregular, resulting from contact wire irregularities, such as hard spots.
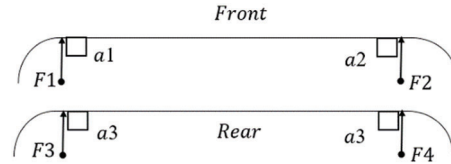

Figure 4: Sensors and accelerometer placement layout

The aerodynamic force was mathematically calculated using Newton's second law and the measured accelerations, with the static lift force being known.

$$F = F_S + F_I + F_L = F_{front} + F_{rear} \tag{2}$$

$$F_{front} = F_1 + F_2 \tag{3}$$

$$F_{rear} = F_3 + F_4 \tag{4}$$

where F is the total measured force value, F_L is the aerodynamic lift force, F_S is the static lift which is between 70–120 N as listed in Table 1, F_I is the impact force which is equal to:

$$F_{I\_front} = m\left(\frac{a_1 + a_2}{2} - g\right) \tag{5}$$

$$F_{I\_rear} = m\left(\frac{a_3 + a_4}{2} - g\right) \tag{6}$$

where m is the mass of the strip, g is the gravitational coefficient, and a is the measured acceleration which is the average of the value measured by both ends.

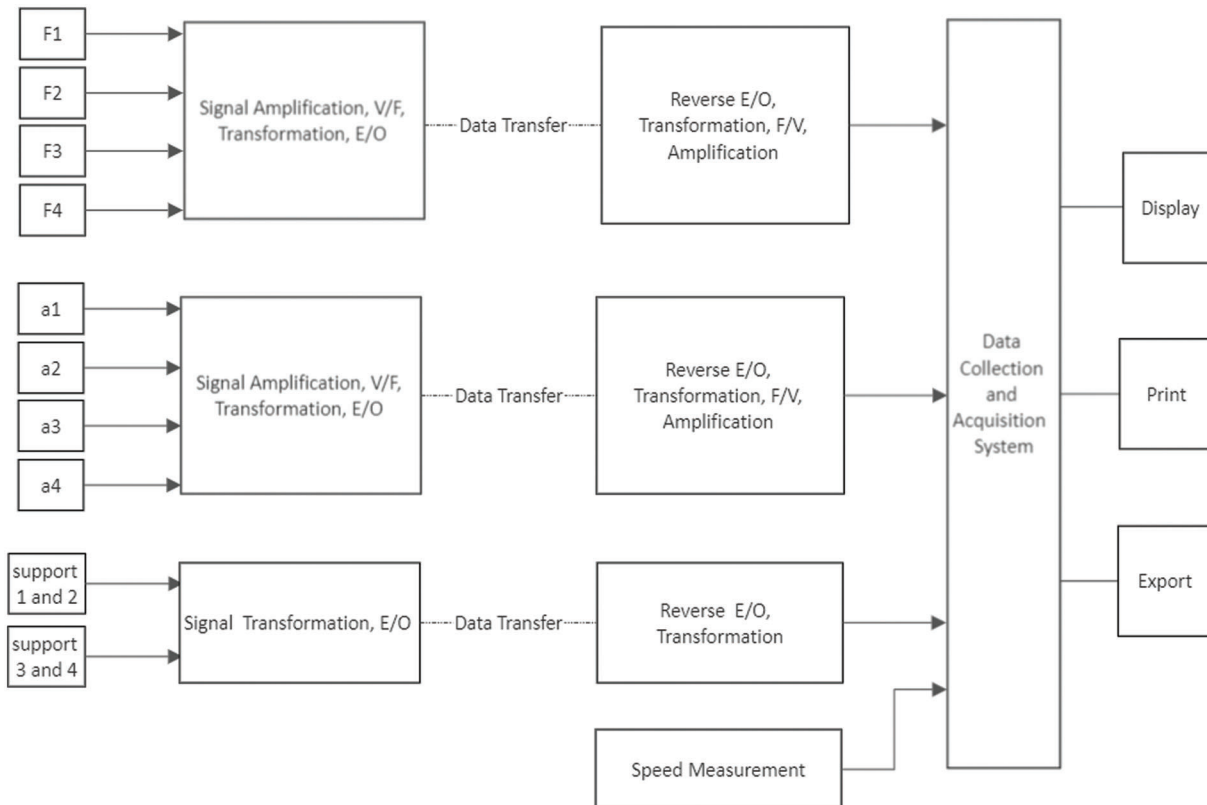The signal processing schematic is shown in Fig. 5.

Figure 5: Data collection system schematics

The experiment was conducted as a full-scale test on an ordinary operating train on a regular operating line between two cities, covering 146.6 km. Sensors were installed on the rear pantograph, which was elevated to its standard operating height during the experiment. The train started from a standstill (0 km/h) and accelerated to a target maximum speed of 350 km/h. Measurements were taken continuously, beginning when the train was at rest and continuing throughout the trip. This real-world test setup was chosen over a wind tunnel experiment to account for the various operational factors and conditions that the pantograph would encounter during its normal use.

The results of the experiment showed that the force acting on the front strip was noticeably higher than the rear strip, as shown in Fig. 6. The test was repeated multiple times on different lines, all of which resulted in similar outcomes.

Subsequently, the wind deflectors were mounted back on, and with the assistance of support technicians sent by the pantograph manufacturer, the position of the deflector was finely tuned for optimal performance. As shown in Fig. 7, the discrepancy in force between the two strips was significantly reduced.
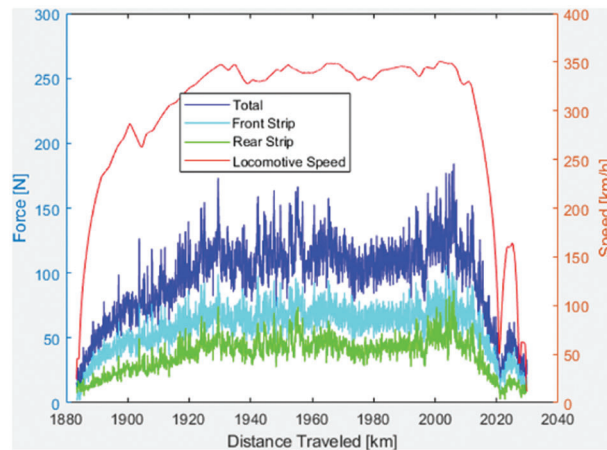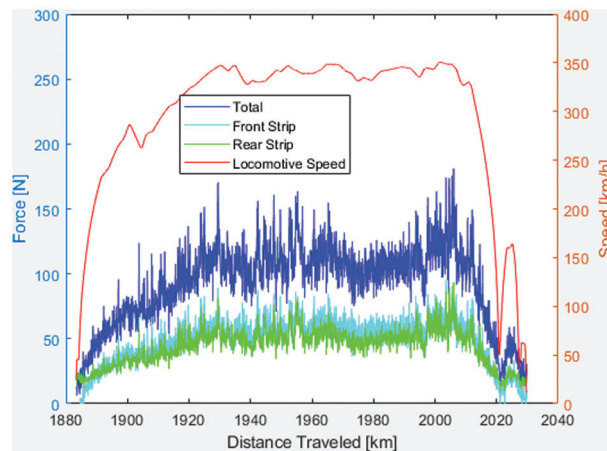
Figure 6: Measurements without deflectors

**Figure 7:** Measurements with deflectors

3 Simulation

To further investigate the performance of the wind deflectors, numerical simulations were conducted using the commercial software ANSYS Fluent. The geometry of the pantograph was modeled based on the specifications listed in Table 1. The computational domain was set up with a length of 50 m, a width of 15 m, and a height of 7.5 m. The pantograph was placed at the center of the domain, with a strip spacing set at 580 mm. The computational domain's inlet was designated as the velocity inlet boundary, with the input flow velocity specified. The outlet of the domain was established as the pressure outlet boundary with a static pressure of 0. The top and both sides of the domain were defined as symmetric boundary conditions, while the pantograph surface and the bottom of the computational domain were assigned as no-slip boundaries. Given that the maximum flow velocity in this investigation does not exceed a Mach number of 0.3, the fluid is assumed to be incompressible.

The setup is illustrated in Fig. 8.

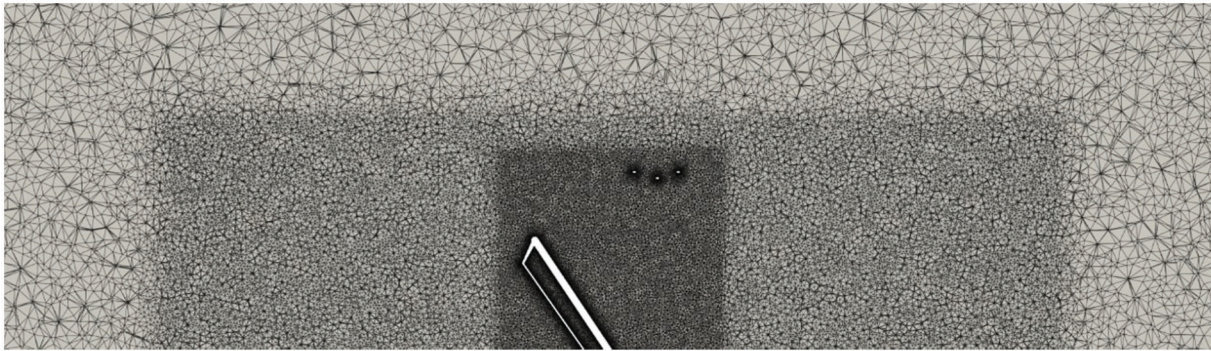**(a)** Pantograph model
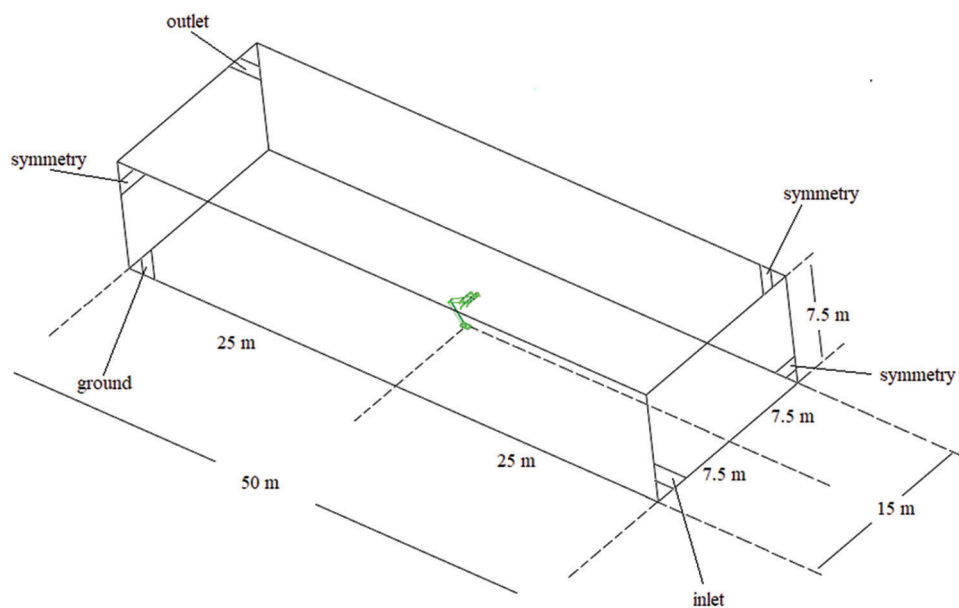
(b) Computational domain

Figure 8: Simulation setup

The grid size was set at 30 mm, resulting in 2.96 million nodes and 2.12 million meshing elements. The boundary layer was set at 15 with a growth rate of 1.2, as illustrated in Fig. 9. The grid size of 180 and 70 mm were less accurate, with 0.71 million nodes and 0.59 million meshing elements, and 1.61 million nodes and 1.16 million meshing elements, respectively. Table 2 presents the overall lift force values for the pantograph without supporting beam wind deflectors at a speed of 350 km/h, derived from three distinct grid sizes. The percentage error was determined by comparing these values against the experimental data, which corresponds to the statistical average of measurements taken at the same speed (114.550 N for 350 km/h).

(a) Pantograph local refinement

(b) Boundary layer

Figure 9: Meshing illustration

Table 2: Mesh sensitivity validation

Grid	Size (mm)	Lift force (N)	Error (%)
Mesh 1	180	128.293	12.0
Mesh 2	70	123.119	7.5
Mesh 3	30	120.357	5.1

The choice of a turbulence model plays a crucial role in the accuracy of the simulation results. Among the most used models in pantograph aerodynamic studies are the k-ε model and the SST k-ω model. The k-ε model has been used in several studies, such as Bocciolone et al. [22], Song et al. [23], Li et al. [24], Li et al. [25], and Arsenea et al. [26]. It is a well-established model that is based on the transport equations for turbulence kinetic energy and its dissipation rate. Another popular model is the SST k-ω model, which has been employed in studies such as Dai et al. [27], Zhang et al. [28], Carnevale et al. [29], Tan et al. [30], Sun et al. [31], Brambilla et al. [32], Kim et al. [33], and Raz et al. [34]. This model is a modified version of the original k-ω model, in which a cross-diffusion expansion is added at the end of the equation using a multiplication factor. This allows the turbulence model to switch between acting as the k-ε model or the original k-ω model for calculations involving flows with a large adverse pressure gradient.

In this study, the SST k-ω model was implemented due to its accuracy and wide application in the field of pantograph aerodynamics. The governing equations are shown below.

Mass equation for an incompressible fluid:

$$\frac{\partial u_i}{\partial x_i} = 0 \tag{7}$$

Momentum equation for an incompressible fluid:

$$\rho \frac{\partial u_i}{\partial t} + \rho \frac{\partial (u_i u_j)}{\partial x_j} = -\frac{\partial p}{\partial x_i} + \frac{\partial \tau_{ij}}{\partial x_j} \tag{8}$$

τ_{ij} is the stress tensor and defined as:

$$\tau_{ij} = (\mu_f + \mu_t) \left(\frac{\partial u_i}{\partial x_j} + \frac{\partial u_j}{\partial x_i} \right) - \frac{2}{3} \rho k \delta_{ij} \tag{9}$$

The SST k-ω model equation:

$$\frac{\partial (\rho k)}{\partial t} + \frac{\partial (\rho u_j k)}{\partial x_j} = P - \beta^* \rho \omega k + \frac{\partial}{\partial x_j} \left[\frac{(\mu_f + \sigma_k \mu_t) \partial k}{\partial x_j} \right] \tag{10}$$

$$\frac{\partial (\rho \omega)}{\partial t} + \frac{\partial (\rho u_j \omega)}{\partial x_j} = \frac{\alpha^* \rho k \omega}{Pk} - \beta \rho \omega^2 + \frac{\partial}{\partial x_j} \left[(\mu_f + \sigma_\omega \mu_t) \frac{\partial \omega}{\partial x_j} \right] \tag{11}$$

where ρ is the fluid density, p is the fluid pressure, δ_{ij} is the Kronecker delta, u_j is the velocity component, μ_f is the fluid dynamic viscosity, μ_t is the turbulent viscosity, P is the turbulence production term, σ_k and σ_ω are the turbulent Prandtl numbers for k and ω, respectively. Parameters β^*, β, and α^* are constants, set at 0.09, 0.075, and 5/9, respectively. Eq. (10) represents the turbulent kinetic energy k, and Eq. (11) describes the specific dissipation rate ω.

The Semi-Implicit Method for Pressure Linked Equations (SIMPLE) approach was selected for the pressure-velocity coupling. The spatial discretization of the momentum, turbulent kinetic energy, and specific dissipation rate equations employed a second-order upwind scheme. Transient simulations were initially conducted to provide the initial field for the convergent steady-state results. A second-order implicit scheme was chosen for temporal discretization, providing better accuracy for transient simulations than first-order schemes. The time step size was set at 10^{-4} s, maintaining the Courant-Friedrichs-Lewy number below 1 to ensure numerical convergence within each time step.

Table 3 shows the simulated results at a flow speed of 350 km/h, along with the experimental results, which correspond to the statistical average of measurements taken at the same speed.

**Table 3:** Simulation and experimental results without deflectors

Location	Lift force (simulation)	Lift force (experiment)
Front strip	71.2217 N	68.2214 N
Rear strip	49.1358 N	46.3285 N
Total	120.357 N	114.550 N

The velocity contour plots depicted in Fig. 10 demonstrate a notable difference in speed between the front and rear strips, with the former exhibiting a higher velocity. This phenomenon can be attributed to the occurrence of boundary layer separation, which involves the detachment of the boundary layer from

the surface, subsequently forming a wake. The separation arises due to an adverse pressure gradient, leading to a decrease in kinetic energy within the boundary layer and ultimately causing it to separate from the surface.
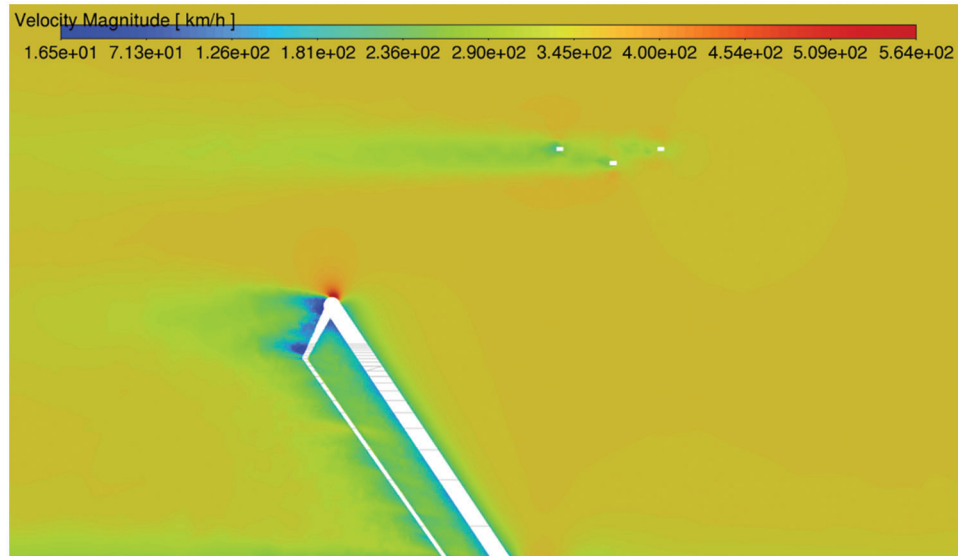
(a) Velocity contour
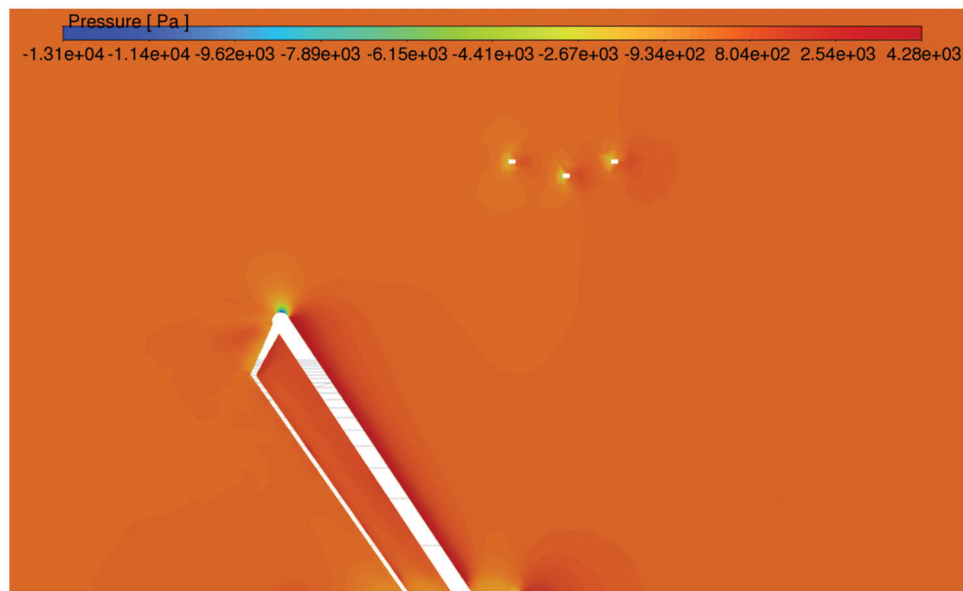
(b) Pressure contour

Figure 10: Contour plots without deflectors

The presence of a reverse flow within the separation zone frequently generates an airflow vortex, contributing to the increased speed of the front strip in comparison to the rear strip. This concept is similarly applicable to the observed increase in velocity at the juncture of the upper and lower arms.

As delineated in Eq. (12), the aerodynamic lift force is directly proportional to the square of the flow velocity. Therefore, the higher speed at the front strip indicates a greater value of lift, which can result in uneven force distribution across the strips. Similarly, the pressure at the front strip is also higher than at the rear strip.

$$F_L = \frac{1}{2} C_L \rho v^2 A \tag{12}$$

where C_L is the lift coefficient, ρ is the density of the fluid, A is the frontal area of the pantograph, and F_L is the lift force.

Next, in the CFD model, wind deflectors were added based on the recommended position by the manufacturers (see Fig. 11). The computational domain and other parameters remained unchanged.
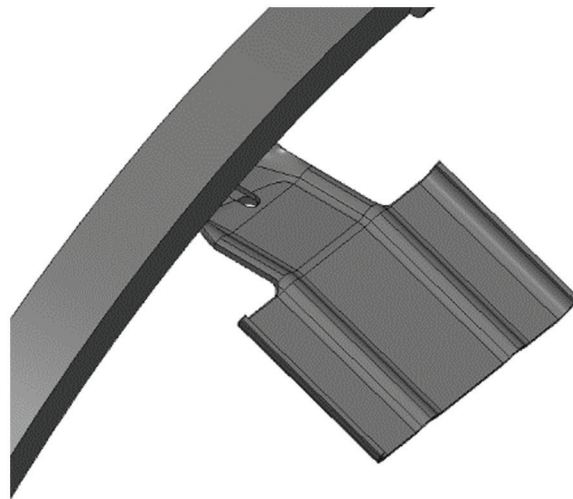

Figure 11: Deflector model

The new simulation results are presented in Table 4 and indicate that the wind deflectors caused a decrease in the force compensation at the front strip, while increasing it at the rear strip. The total lift force remained slightly lower than in the previous simulation without the deflectors. The experimental outcomes are included as well to facilitate a comparison between the two sets of results.

**Table 4:** Simulation and experimental results with deflectors

Location	Lift force (simulation)	Lift force (experiment)
Front strip	61.1276 N	58.5542 N
Rear strip	56.0943 N	53.6614 N
Total	117.222 N	112.215 N

The corresponding contour plots in Fig. 12 demonstrate a more balanced velocity and pressure distribution between the two strips with the wind deflectors installed. The velocity contour plot in Fig. 12a shows a reduced velocity differential between the front and rear strips, indicating that the wind deflectors helped to mitigate the airflow separation issue observed in the previous simulation. Similarly,

the pressure contour plot in Fig. 12b shows a more uniform pressure distribution across the strips with the deflectors, indicating a more effective flow control.
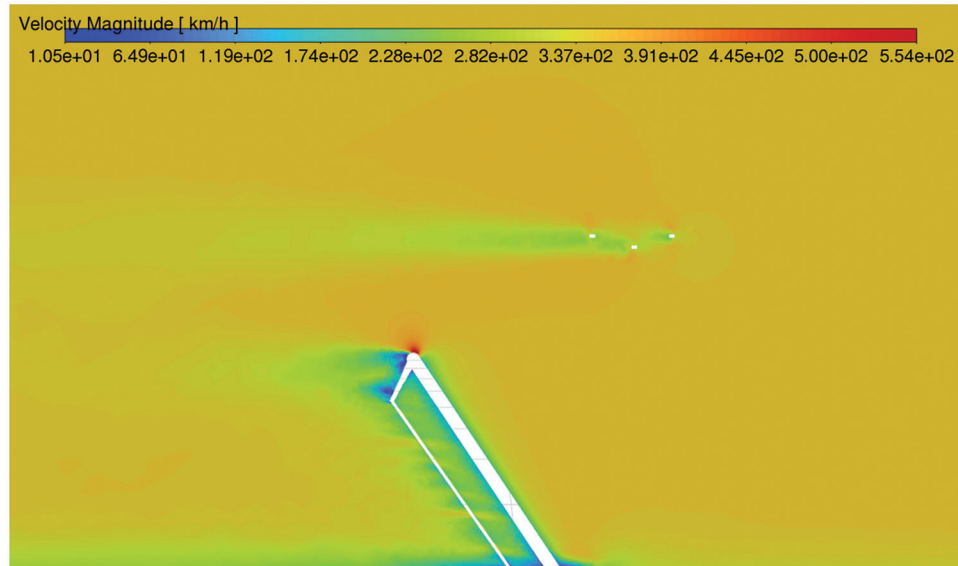
(a) Velocity contour
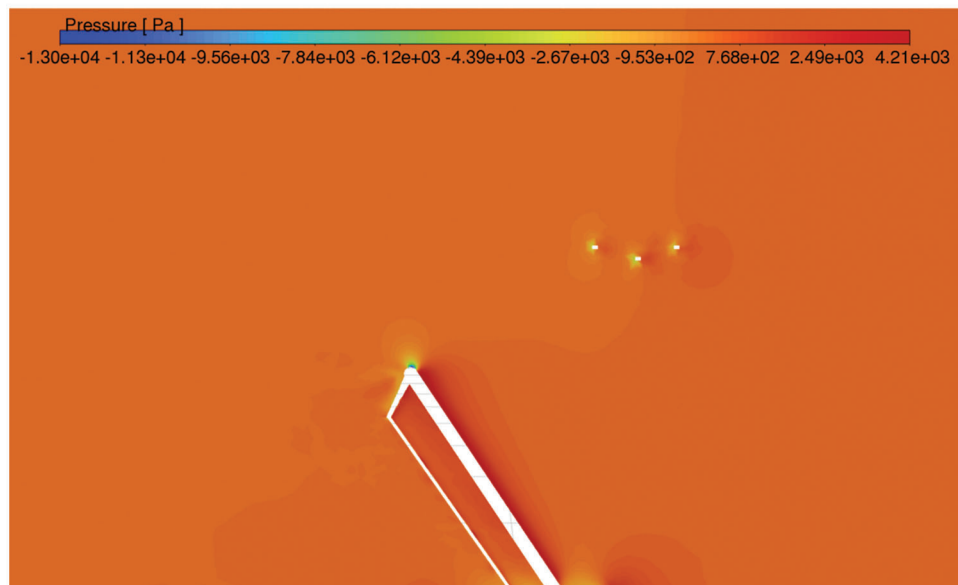
(b) Pressure contour

Figure 12: Contour plots with deflectors

In Fig. 13, the pressure streamline plot shows the effect of the wind deflectors on the airflow around the pantograph. The streamline's pattern illustrates how the deflectors redirect the airflow and reduce the turbulence near the strips, resulting in a more balanced pressure distribution across the strips. These simulation results demonstrate that the wind deflectors have a positive impact on the aerodynamic performance of the pantograph.
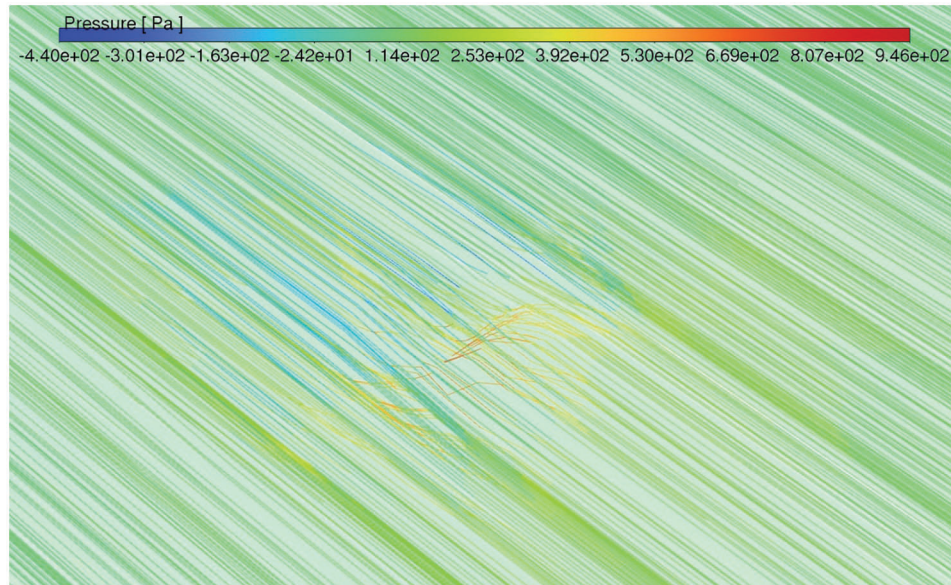
Figure 13: Deflector pressure streamline plot

4 Optimization

For optimization, various factors such as installation direction, shift range, and size are considered. The options available for the supporting beam deflectors during operation are limited to installation direction (upwards, downwards, or removal) and sliding screw position adjustments. The installation direction affects the compensation of the aerodynamic lift, as demonstrated in Fig. 14. A "π" shaped installation with the front deflector facing downwards and the rear deflector facing upwards is commonly used.

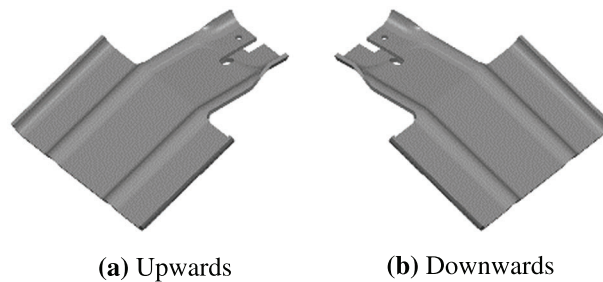**(a)** Upwards   **(b)** Downwards

Figure 14: Deflector installation directions

In addition, the shift range of the deflectors is also a crucial factor, with a shift range of only approximately 1.3 cm for the particular type of pantograph studied in this article. However, in the simulation, a maximum shift range of 3 centimeters was assumed, as shown in Fig. 15.

The size of the wind deflector is another important consideration, as the force compensated is proportional to the area of the deflector, as illustrated in Table 5 and Fig. 16.

A lift compensation of approximately 22 N is required for the pantograph used in this study, and feasible deflector sizes are listed in Table 6. It is important to note that the overall aerodynamic characteristics of the pantograph must also be considered during design. For example, the size of the deflectors in the downwards

orientation should not exceed that in the upwards orientation to reduce the overall aerodynamic lift. By considering all these factors, the wind deflectors can be optimized to achieve the desired performance.
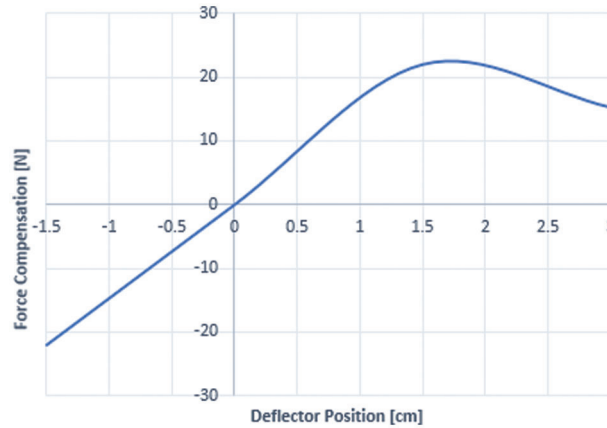

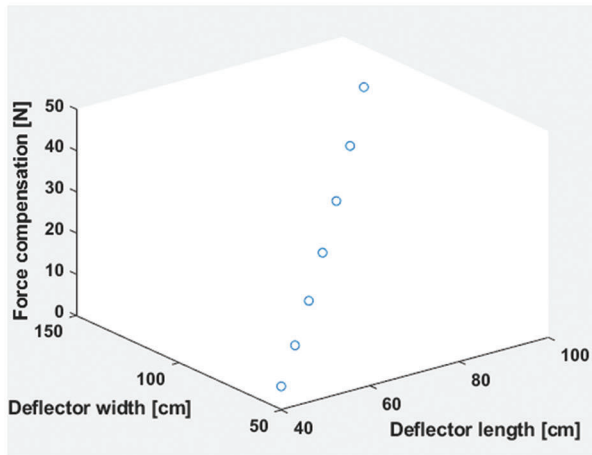**Figure 15:** Lift compensation *vs*. deflector position

Table 5: Lift compensation *vs*. size results at 1.3 cm

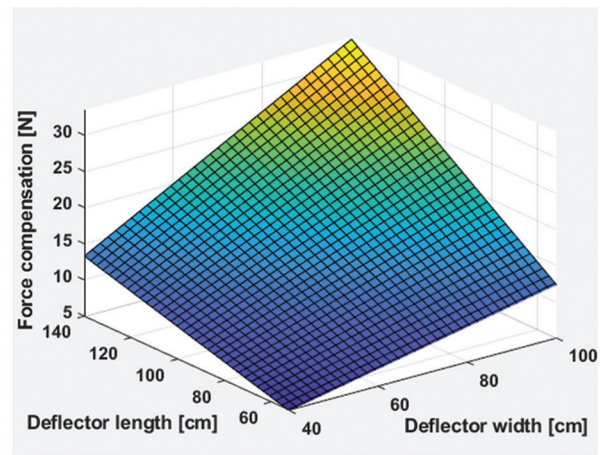| Size	Upwards	Downwards
40 cm × 50 cm	4.748 N	−5.761 N
50 cm × 70 cm	8.310 N	−10.08 N
70 cm × 80 cm	13.29 N	−16.13 N
80 cm × 100 cm	18.98 N	−23.04 N

5 Alternatives to Deflectors

The use of wind deflectors is not the only approach available to address pantograph aerodynamics. One alternative is to use control circuits in place of or in conjunction with wind deflectors. Both passive and open-loop active control valves have already been adopted with some pantograph models. The closed-loop active control valve is still under development and involves sending force and acceleration measurement data to a control unit, which then calculates the amount of pressure compensation required to achieve the target lift force value. A proportional valve or high-frequency regulator then responds accordingly. However, this approach presents certain challenges such as the high cost of customized sensors, difficulty in data collection in a high-speed environment, and the high precision control requirement for the hysteresis drive system.

Another alternative is the use of a single-strip pantograph (see Fig. 17), which only has one strip, eliminating the problem of uneven pressure between strips. Additionally, it is lightweight and compact in size, which facilitates maintenance and reduces impact force as per Eqs. (5) and (6). However, single-strip pantographs have less electrical redundancy and are structurally weaker than double-strip pantographs. Therefore, railway operators need to weigh the pros and cons when selecting the most suitable pantograph type and wind compensation strategy for their operations.
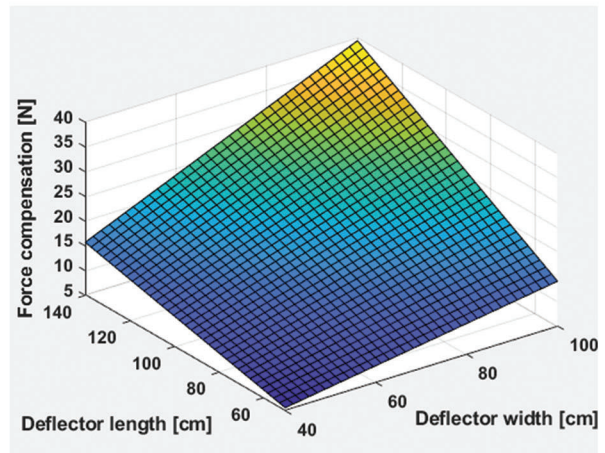
(a) Upwards 3D plot

(b) Upwards surface plot
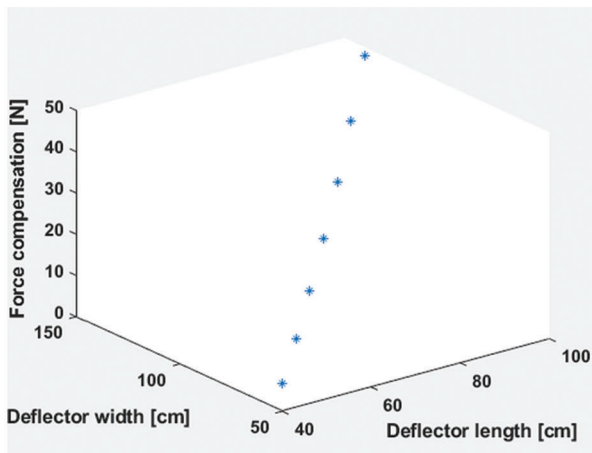
(c) Downwards 3D plot

(d) Downwards surface plot

Figure 16: Lift compensation *vs.* size plot at 1.3 cm

Table 6: Examples of feasible sizes for deflector pairs

Option	Rear deflector	Front deflector	Total compensation
1	60 cm × 70 cm	60 cm × 70 cm	21.77 N
2	70 cm × 80 cm	50 cm × 60 cm	21.76 N
3	90 cm × 100 cm	Not installed	21.37 N
4	Not installed	80 cm × 95 cm	21.36 N

It is essential to consider all possible alternatives and their advantages and disadvantages when optimizing pantograph aerodynamics. The decision must be based on a thorough understanding of the trade-offs between different approaches, considering their specific requirements in terms of cost, reliability, and performance. Additionally, it is essential to consider the potential impact of external

factors such as operating speed. A comprehensive optimization process that considers all of these factors is necessary to ensure optimal current collection performance for the pantograph-catenary system.
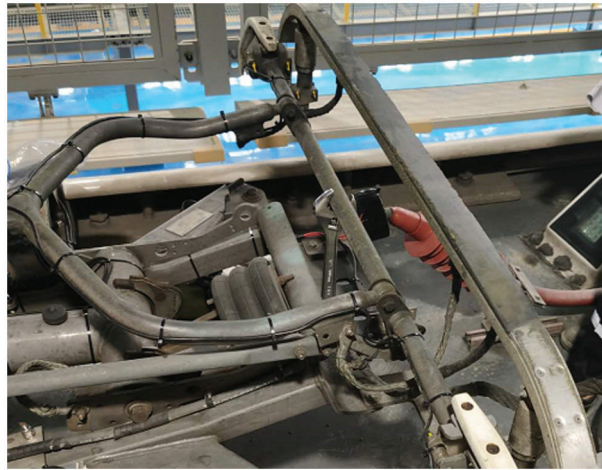

Figure 17: Single-strip pantograph

6 Conclusion

This study provides a comprehensive understanding of the aerodynamic properties of high-speed pantographs equipped with supporting beam wind deflectors, based on both experimental and numerical analyses. The key findings and recommendations are summarized below:

(1) Proper installation and configuration of supporting beam wind deflectors contribute to a more balanced lift force distribution between the front and rear strips. The lift force on the front strip decreases by 9.67 N, while it increases on the rear strip by 7.33 N, resulting in a reduction in the lift force difference from 22 to 4.9 N. The numerical results are in close agreement with the experimental measurements, and both sets of data demonstrate a reduced force difference.

(2) Optimal aerodynamic performance can be achieved by considering various factors, including deflector size, position, and installation orientation. A "π" shaped configuration, where the front strip deflectors are installed downwards and the rear strip deflectors upwards, is recommended. Four possible solutions for 22 N force compensation are: 60 cm × 70 cm rear deflectors combined with 60 cm × 70 cm front deflectors, 70 cm × 80 cm rear deflectors combined with 90 cm × 100 cm front deflectors, 90 cm × 100 cm rear deflectors only, or 80 cm × 95 cm front deflectors only.

(3) While using wind deflectors is an effective approach for compensating lift forces, it is essential to evaluate other alternatives based on operational needs. Railway operators should weigh the pros and cons of different pantograph types and wind compensation strategies to ensure optimal current collection performance for the pantograph-catenary system.

Author Contributions: The authors confirm contribution to the paper as follows: study conception and design: Shiyang Song; data collection: Tongxin Han; analysis and interpretation of results: Shiyang Song;

draft manuscript preparation: Shiyang Song. All authors reviewed the results and approved the final version of the manuscript.

References

1. Pombo, J., Ambrósio, J., Pereira, M., Rauter, F., Collina, A. et al. (2009). Influence of the aerodynamic forces on the pantograph-catenary system for high-speed trains. *Vehicle System Dynamics, 47(11),* 1327–1347.

2. AbdelGawad, A., Aljameel, N., Shaltout, R. (2022). Computational modelling of the aerodynamic noise of the full-scale pantograph of high-speed trains. *Journal of Advanced Research in Fluid Mechanics and Thermal Sciences, 93(1),* 94–109.

3. Li, H., Liu, X., Thompson, D., Squicciarini, G. (2022). The distribution of pantograph aerodynamic noise on train external surfaces and the influence of flow. *Applied Acoustics, 188,* 108542.

4. Tan, J., Bai, B., Xu, X., Yang, X. (2017). Numerical computation for the impact of pantograph angles on the near-field and far-field aerodynamic noises of pantographs. *Journal of Vibroengineering, 19(8),* 6471–6484.

5. Yan, Y., Xu, X., Wang, X., Geng, H., Huang, S. (2022). Simulation optimization study on aerodynamic drag reduction of high-speed pantograph. *Mechanics in Engineering, 44(2),* 276–284.

6. Cheng, J., Guo, D., Yang, G., Ji, Z., Chen, D. (2022). Research on effects of tunnel buffer structures on the aerodynamic force of the pantograph. *Proceedings of the ASME, 2022 Fluids Engineering Division Summer Meeting*, Toronto, Canada.

7. Dai, Z., Li, T., Zhou, N., Zhang, J., Zhang, W. (2022). Effect of upper and lower arms diameters on aerodynamic uplift force of high-speed pantograph. *Journal of Traffic and Transportation Engineering, 22(4),* 210–222.

8. Watroba, P. (2015). Numerical simulation of aerodynamic forces which have an impact on the pantograph. *21st International Conference Engineering Mechanics*, Svratka, Czech Republic.

9. Vo-Van, O., Massat, J., Laurent, C., Balmes, E. (2014). Introduction of variability into pantograph-catenary dynamic simulations. *Vehicle System Dynamics, 52(10),* 1254–1269.

10. Shaltout, R., Aljameel, N., Abdelgawad, A. (2022). Modeling and simulation of the aerodynamic noise of high-speed train's pantograph. *Journal of Engineering, 2022,* 1164017.

11. Mitsumoji, T., Sueki, T., Yamazaki, N., Sato, Y., Ikeda, M. et al. (2015). Aerodynamic noise reduction of a pantograph panhead by applying a flow control method. *Noise and Vibration Mitigation for Rail Transportation Systems, 126,* 515–522.

12. Siano, D., Viscardi, M., Donisi, F., Napolitano, P. (2014). Numerical modeling and experimental evaluation of an high-speed train pantograph aerodynamic noise. *5th International Conference on Automotive and Transportation Systems (ICAT 14)*, Cambridge, USA.

13. Ikeda, M., Manabe, K. (2000). Development of low noise pantograph with passive lift suppression mechanism of panhead. *Quarterly Report of RTRI, 41(4),* 177–181.

14. Collina, A., Facchinetti, A., Resta, F. (2007). A feasibility study of an aerodynamic control for a high speed pantograph. *2007 IEEE/ASME International Conference on Advanced Intelligent Mechatronics*, Zurich, Switzerland.

15. Kim, H., Hu, Z., Thompson, D. (2020). Effect of cavity flow control on high-speed train pantograph and roof aerodynamic noise. *Railway Engineering Science, 28,* 54–74.

16. Li, T., Deng, Q., Zhang, W., Zhang, J. (2020). Study on the aerodynamic noise characteristics of high-speed pantographs with different strip spacings. *Journal of Wind Engineering and Industrial Aerodynamics, 202,* 104191.

17. Dai, Z., Li, T., Deng, J., Zhou, N., Zhang, W. (2022). Effect of the strip spacing on the aerodynamic performance of a high-speed double-strip pantograph. *Vehicle System Dynamics, 60(10),* 3358–3374.

18. Dai, Z., Li, T., Zhang, W., Zhang, J. (2020). Numerical study on aerodynamic performance of high-speed pantograph with double strips. *Fluid Dynamics & Materials Processing, 16(1),* 31–40. https://doi.org/10.32604/fdmp.2020.07661

19. Shi, J., Ge, S., Sheng, X. (2021). Numerical investigation on the aerodynamic noise generated by a simplified double-strip pantograph. *Fluid Dynamics & Materials Processing, 18(2),* 463–480. https://doi.org/10.32604/fdmp.2022.017508

20. Dai, Z., Li, T., Zhou, N., Zhang, J., Zhang, W. (2021). Numerical simulation and optimization of aerodynamic uplift force of a high-speed pantograph. *Railway Engineering Science, 30,* 117–128.

21. Maaß, J. (2021). Insulator for a rail vehicle and pantograph. Germany, DE102019121932A1. https://register.dpma.de/DPMAregister/pat/PatSchrifteneinsicht?docId=DE102019121932A1

22. Bocciolone, M., Resta, D., Rocchi, A., Tosi, A., Collina, A. (2007). Pantograph aerodynamic effects on the pantograph-catenary interaction. *Vehicle System Dynamics, 44,* 560–570.

23. Song, Y., Liu, Z., Wang, H., Lu, X., Zhang, J. (2016). Nonlinear analysis of wind-induced vibration of high-speed railway catenary and its influence on pantograph-catenary interaction. *Vehicle System Dynamics, 54(6),* 723–747.

24. Li, R., Zhang, W., Zhou, N., Liu, B., Zou, D. et al. (2016). Influence of a high-speed train passing through a tunnel on pantograph aerodynamics and pantograph-catenary interaction. *Proceedings of the Institution of Mechanical Engineers, Part F: Journal of Rail and Rapid Transit, 231(2),* 198–210.

25. Li, R., Zhou, N., Zhang, W., Mei, G., Chen, Z. (2012). Calculation method and analysis of pantograph aerodynamic lifting force. *Journal of the China Railway Society, 34(8),* 26–32.

26. Arsenea, S., Sebesan, I., Popaa, G. (2014). The influence of wind on the pantograph placed on the railway electric vehicles bodywork. *5th World Conference on Learning Teaching and Educational Leadership (WCLTA 2014)*, Prague, Czech Republic.

27. Dai, Z., Li, T., Zhou, N., Zhang, J., Zhang, W. (2022). Numerical simulation and optimization of aerodynamic uplift force of a high-speed pantograph. *Railway Engineering Science, 30,* 117–128.

28. Zhang, L., Zhang, J., Li, T., Zhang, W. (2017). Influence of pantograph fixing position on aerodynamic characteristics of high-speed trains. *Journal of Modern Transportation, 25,* 34–39.

29. Carnevale, M., Facchinetti, A., Rocch, D. (2017). Procedure to assess the role of railway pantograph components in generating the aerodynamic uplift. *Journal of Wind Engineering and Industrial Aerodynamic, 160,* 16–29.

30. Tan, X., Xie, P., Yang, Z., Gao, J. (2019). Adaptability of turbulence models for pantograph aerodynamic noise simulation. *Shock and Vibration, 5,* 1–20.

31. Sun, Z., Yao, S., Wei, L., Yao, Y., Yang, G. (2021). Numerical investigation on the influence of the streamlined structures of the high-speed train's noise on aerodynamic performances. *Applied Science, 11(2),* 784.

32. Brambilla, E., Carnevale, M., Facchinetti, A., Rocchi, D. (2022). Influence of train roof boundary layer on the pantograph aerodynamic uplift: A proposal for a simplified evaluation method. *Journal of Wind Engineering and Industrial Aerodynamics, 231,* 105212.

33. Kim, H., Hu, Z., Thompson, D. (2020). Numerical investigation of the effect of cavity flow on high speed train pantograph aerodynamic noise. *Journal of Wind Engineering and Industrial Aerodynamics, 201,* 104159.

34. Raz, L., Zahalka, M., Chval, Z. (2016). Reduction of pantograph influence on energy consumption. *Proceedings of the 27th DAAAM International Symposium*, Vienna, Austria.